

Bias driven circular current in a ring nanojunction: Critical role of environmental interaction

Moumita Mondal¹ and Santanu K. Maiti^{1,*}

¹*Physics and Applied Mathematics Unit, Indian Statistical Institute,
203 Barrackpore Trunk Road, Kolkata-700 108, India*

(Dated: April 10, 2025)

The specific role of environmental interaction on bias driven circular current in a ring nanojunction is explored within a tight-binding framework based on wave-guide theory. The environmental interaction is implemented through disorder in backbone sites where these sites are directly coupled to parent lattice sites of the ring via single bonds. In absence of backbone disorder circular current becomes zero for a lengthwise symmetric nanojunction, while it increases with disorder which is quite unusual, and after reaching a maximum it eventually drops to zero in the limit of high disorder. The effects of ring-electrode interface configuration, ring-backbone coupling, different types of backbone disorder and system temperature are critically investigated. All the studied results are valid for a broad range of physical parameters, giving us confidence that the outcomes of this theoretical work can be verified experimentally. To make this study self-contained, we also discuss the feasibility of detecting bias-driven circular current and provide design guidelines for implementing our proposed quantum system in a laboratory.

I. INTRODUCTION

Nano rings have long been the focus of intense research, revealing numerous fascinating phenomena compared to linear counterparts. When a loop conductor interfaces with external electronic baths, it generates a net circular current under specific conditions¹⁻⁵. While researchers are familiar with transport or junction currents⁶⁻⁹, bias-driven circular currents represent a relatively novel phenomenon that has yet to be thoroughly investigated. Some groups¹⁻⁵ have made attempts in this direction previously, but it was the pioneering work of Nitzan and his team^{10,11} around a decade ago that brought it to prominence. Circular currents involve current distributions within individual bonds, leading to the emergence of crucial features such as the conducting properties of multi-arm loop systems, the specific role of disorder, and the nature of total current flow.

The majority of literature articles have primarily explored the phenomenon of circular currents in nanojunctions under voltage bias, typically assuming disorder-free conductors^{1-5,10-14}. Little attention has been paid to discussing the influence of disorder^{15,16}. *However, the impact of environmental interactions, which are often unavoidable in experimental settings, has not been well investigated.* Our current study aims to fill this gap. To address this, we examine a nano ring positioned between source and drain electrodes, with each ring site directly linked to a backbone site (refer to Fig. 1). The environmental interaction is introduced phenomenologically by incorporating impurities into these backbone sites¹⁷⁻²³. This protocol is a standard method for assessing how the environment interacts with the system, and it has been utilized in numerous studies concerning transport phenomena. Various types of disorder can be considered. It can either be fully uncorrelated (random)²⁴⁻²⁸, which is commonly employed, or correlated (non-random)²⁹⁻⁴⁶. Random disorder is relatively straightforward but requires extensive configuration averaging across numerous distinct configurations. Conversely, with correlated dis-

order, configuration averaging is unnecessary, and many nontrivial signatures emerge. One captivating example of correlated disorder is the Aubry-André-Harper (AAH) model³⁰⁻³⁵, renowned for its diverse and intriguing characteristics, which has been extensively explored in various contexts.

In this study, we incorporate disorder in backbone sites following the AAH form and explicitly discuss its effect

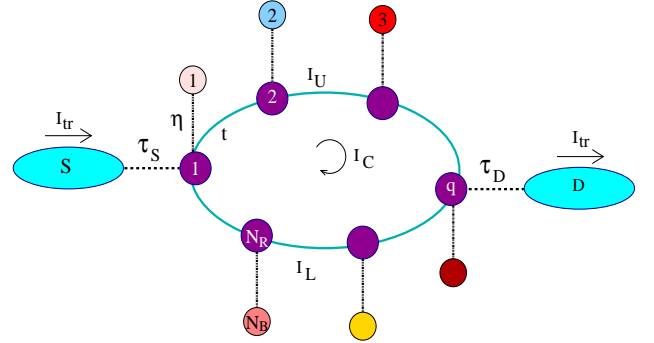


FIG. 1: (Color online). Schematic diagram of the junction setup where a nano ring is attached to source and drain electrodes. Each site of the ring is connected to a backbone site via a single bond. In presence of finite bias between source (S) and drain (D), a net circular current, I_C , appears in the ring. I_{tr} represents the transport current, commonly referred to as the junction current. Disorder is introduced at the backbone sites while keeping the ring sites clean.

on bias-driven circular current. Using a tight-binding (TB) framework to illustrate the nanojunction, we obtain the circular current based on the well-known wave-guide (WG) theory^{13,15}. Interestingly, we observe that the ‘bias driven circular current’ increases with disorder strength. After reaching a maximum, the current decreases and practically drops to zero in the limit of high disorder strength. Thus, backbone disorder, representing environmental interaction, effectively enhances the circular current within a specific region, which is quite important in the context of circular current in a loop

nanojunction. Here, it is relevant to note that disorder-assisted transport phenomena have been explored^{47,48} in different other quantum systems, revealing the fact that disorder can enhance transport current. Considering a tight-binding one-dimensional chain with random side sites, Xiong has shown⁴⁹ with simple mathematical analysis and clear physical arguments that conduction can be improved with increasing the disorder strength. This argument matches well with the analysis done by Zhong *et al.*⁵⁰ in their work where they have considered shell-doped nanowires in which dopant atoms are distributed in some regions, leaving other parts undoped. As the doping concentration increases, conduction improves, unlike to fully disordered systems. Several atypical signatures are expected when a perfect conductor is coupled to a disordered region, differing from those seen in a fully disordered system. To make our present study comprehensive, along with disorder, we also critically investigate the effects of (i) ring-electrode junction configuration, which plays a dominant role in transport behavior, (ii) ring-backbone coupling, (iii) other types of disorder, and (iv) system temperature. Our detailed numerical calculations reveal that environmental interaction has a strong effect on circular current.

We organize our work as follows. After the brief introduction above, in Sec. II we present the ring nanojunction, its tight-binding Hamiltonian, and the necessary theoretical steps for obtaining the results. In a separate appendix some additional mathematical steps are given for better understanding. In Sec. III, we critically explain all the findings with appropriate physical arguments. In addition, we explore the possibilities of detecting bias driven circular current and provide design prescriptions for implementing our proposed quantum system in a laboratory. Finally, we conclude in Sec. IV.

II. JUNCTION SETUP, HAMILTONIAN AND THEORETICAL FRAMEWORK

A. Nanojunction and the TB Hamiltonian

Let us start with the junction setup shown in Fig. 1. A one-dimensional nano ring, possessing N_R lattice sites, is clamped between two electron reservoirs, commonly referred to as source (S) and drain (D). Each lattice site of the ring (represented by a filled purple circle) is connected to a backbone site via a single bond. To denote backbone sites are disordered, we use different colors for those sites. The total number of backbone sites is mentioned by the parameter N_B , and in our setup N_B is always identical to N_R . Once a bias is applied across the electrodes, a transport current (I_{tr}), more commonly referred to as junction current, is generated. This current splits into two arms of the ring and reunite at the drain end. Along with the transport current, a net circular current, specified by I_c , can be induced in the ring, under suitable conditions. While the behavior of the transport current is well understood, the characteristic features of bias-driven circular current remain relatively unexplored. This study aims to investigate these aspects.

The ring-electrode junction system is simulated within a tight-binding framework. Since the complete system contains different parts, it is convenient to write the full Hamiltonian, H , as a sum of different sub-Hamiltonians related to different parts of the junction and the associated coupling, viz, ring, source, drain and the coupling between ring and electrodes^{13,15}. The general form of TB Hamiltonian of any part within nearest-neighbor hopping (NNH) approximation looks like

$$H_\beta = \sum_n \epsilon_{\beta,n} c_{\beta,n}^\dagger c_{\beta,n} + \sum_n t_\beta (c_{\beta,n}^\dagger c_{\beta,n+1} + h.c.) \quad (1)$$

where $\beta = S, D, \text{ ring (R) and backbone (B)}$. $\epsilon_{\beta,n}$ corresponds to the on-site energy of an electron at site n of the part β and t_β is the NNH strength. Now we explicitly mention these TB parameters associated to different parts of the junction. For the side-attached electrodes we set $\epsilon_{\beta,n} = \epsilon_0$ and $t_\beta = t_0$. The electrodes are assumed to be one-dimensional, reflection-less and perfect. The source and drain are coupled to the ring via the coupling parameters τ_S and τ_D , respectively. In the junction setup, it is considered that the source is always connected to site number 1 of the ring, while the drain position (site number q) can vary (see Fig. 1). The physical system sandwiched between source and drain contains two different kinds of sites: sites associated to the ring (those are referred to parent lattice sites) and the backbone sites. Any ring site is labeled as $\epsilon_{R,n}$ and for the backbone site it is $\epsilon_{B,n}$. In our setup the ring sites are clean (viz, all the ring sites are identical), and disorder is introduced only in the backbone sites. Unless specified, we choose $\epsilon_{B,n}$ in the form of AAH model³²⁻³⁵

$$\epsilon_{B,n} = W \cos(2\pi b n) \quad (2)$$

where W is the disorder strength and b is an irrational number. Here, the site index n runs over all the backbone sites, i.e., from 1 to N_B . As pointed out, another type of disorder can also be taken into account. Each backbone site is connected to a parent lattice site via a single bond with the hopping strength η . For the case of rational b , the backbone sites become perfect and the periodicity depends on the choice of b and N_B . The NNH strength in the ring is mentioned by the parameter t .

B. Theoretical Prescription

To understand the description of circular current, let us start with arm currents associated with different arms of the ring geometry. For our chosen setup, if the upper and lower arms having the lengths L_U and L_L carry the currents I_U and I_L respectively then the circular current, I_c , is defined as¹⁰⁻¹²

$$I_c = \frac{I_U L_U + I_L L_L}{L_U + L_L} \quad (3)$$

where L (circumference of the ring) = $L_U + L_L$. When the lengths and status of the two arms are exactly identical it is simple to follow that $I_U = -I_L$ and then I_c becomes

zero. So, in order to have a non zero I_c we need to break the symmetry between the two arms. The symmetry breaking can be done in three ways: (i) by changing the arm lengths or (ii) by setting the status of the two arms different when their lengths are identical or (iii) by both. In our case, we set all those conditions one by one.

In TB framework the current in any arm or any single/multiple bonds can be calculated by using the WG theory (a standard protocol)^{13,15}. For that first we need to calculate the bond current densities in individual bonds. The current density in any bond of the ring is defined as¹⁰⁻¹³

$$J_{n,n+1}(E) = \left(\frac{2e}{\hbar}\right) \text{Im} [tC_{R,n}^* C_{R,n+1}] \quad (4)$$

where t is the NNH strength in the ring (mentioned earlier), e and $\hbar (= h/2\pi)$ carry their usual meanings; $C_{R,n}$'s are the wave amplitudes, and they are evaluated by solving $(N_R + N_B + 2)$ coupled equations (for more details, we suggest to see Refs.^{13,15}). The general form of the coupled equations look like

$$(E - \epsilon_{\beta,n})C_{\beta,n} = \sum_m t_{\beta,m} C_{\beta,m} \quad (5)$$

where m is the site index referring to the nearest-neighbor sites of n . The $(N_R + N_B)$ equations come from the ring and backbone sites, and other two equations arise from the sites where the ring is coupled to S and D. For a complete understanding of these coupled equations, refer to Appendix A, where all equations are explicitly written for a ring nanojunction. Once the coefficients, $C_{\beta,n}$, associated with the lattice sites are obtained, we can determine all the bond current densities. By summing over the relevant bonds, we can compute the current densities associated with upper and lower arms, denoted as J_U and J_L , respectively.

Integrating current densities over a suitable energy window we find the currents, as a function of voltage, associated with different arms. The arm current is expressed as¹⁰⁻¹³

$$I_{U/L} = \int J_{U/L}(E)(f_S - f_D) dE \quad (6)$$

where $f_{S(D)}$ is the Fermi-Dirac distribution function for S(D), and it is

$$f_{S(D)} = \frac{1}{1 + e^{\frac{(E - \mu_{S(D)})}{K_B T}}}. \quad (7)$$

Here T is the equilibrium temperature, K_B is the Boltzmann constant, and μ_S and μ_D are the electro-chemical potentials of S and D respectively. In terms of the equilibrium Fermi energy E_F and bias voltage V , μ_S and μ_D are written as: $\mu_S = E_F + eV/2$ and $\mu_D = E_F - eV/2$. Once I_U and I_L are found out, the circular current I_c is obtained from the above mentioned definition (Eq. 3).

III. RESULTS AND DISCUSSION

The central focus of this work is to investigate the specific role of backbone disorder on bias driven circular cur-

rent in a nano ring. Unless mentioned, the disorder is introduced in backbone sites in the cosine form following the AAH model. The incommensurate factor ' b ' in the expression of $\epsilon_{B,n}$ is chosen as $(1 + \sqrt{5})/2$ (golden mean) which is quite common for the AAH model and has been used extensively in the literature^{35,51}, though any other irrational number can be taken into consideration. At the end of this section, the effects of other two types of correlated disorders on I_c are also discussed to check the sensitivity of I_c on the nature of the disorder. The results are mostly discussed for the lengthwise symmetric ring nanojunction, setting the temperature at zero Kelvin. The effects of ring-electrode junction configuration, ring-backbone coupling and temperature are studied in appropriate parts for the sake of completion.

For computing the results, the values of some of the physical parameters are kept constant throughout the work, and here it is relevant to mention them. If not

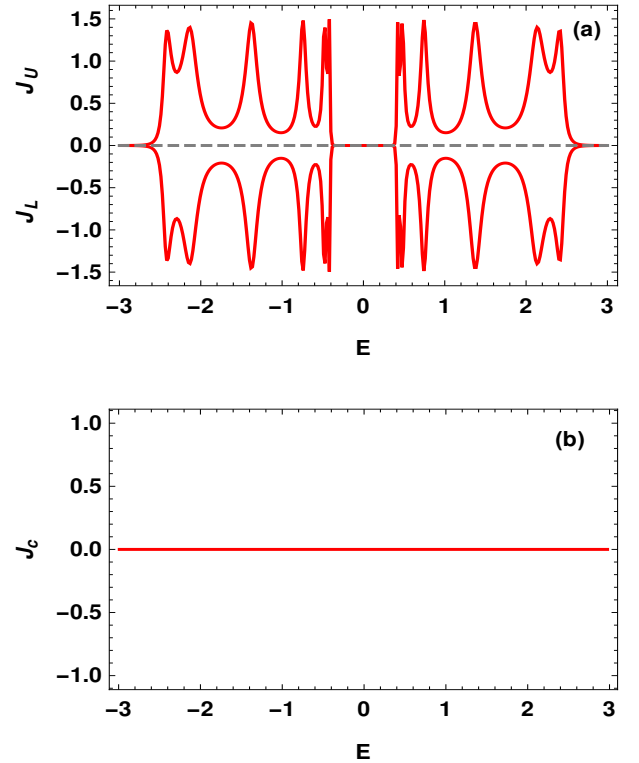


FIG. 2: (Color online). Variation of (a) J_U and J_L and (b) total current density $J_c (= J_U + J_L)$ as a function of energy E for a 10-site ring in the absence of any disorder ($W = 0$) on backbone sites. The upper and lower arms are identical in length.

indicated otherwise, we set $\epsilon_0 = 0$, $t_0 = 3$, $\tau_S = \tau_D = 1$, $\epsilon_{R,n} = 0$, $t = 1$, $\eta = 1$, $E_F = 0$, $T = 0$ and $N_R = 10$. The values of other TB parameters that are not fixed, are specified as needed during the discussion. All energies are measured in units of eV, and currents are determined in units of mA.

Let us now begin our discussion and analyze the results step by step. To understand the impact of backbone disorder it is indeed meaningful to start with the setup where all the backbone sites are free from any disorder,

which is obtained by setting $W = 0$, and to check the dependence of current densities associated with the upper and lower arms of the ring, as well as the circular current density. The results are presented in Fig. 2 where the characteristic behaviors of J_U and J_L are shown in (a), and in (b), the variation of the circular current density J_c is depicted. J_c is obtained by summing J_U and J_L . Several important features are evident. Both for J_U and J_L we have finite peaks around some energies and for other energies they are vanishingly small. For a small window across $E = 0$, the current densities vanish completely. These peaks in the current density profiles are associated

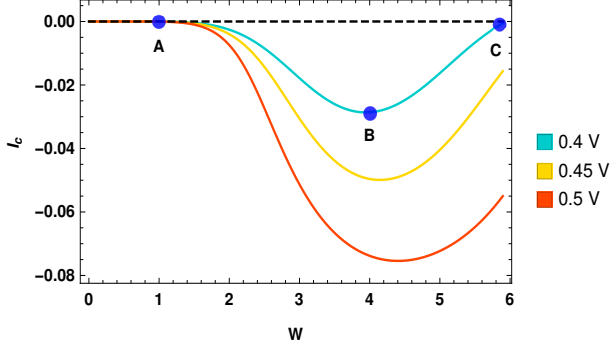


FIG. 3: (Color online). Circular current I_c as a function of backbone disorder strength W for three distinct voltages, denoted by three different colored curves, for a 10-site ring. Three dot points, A, B and C, on the cyan curve are highlighted to specify the three different values of W (low, moderate and high), where the nature of I_c is critically investigated.

with the energy eigenvalues of the ring-backbone system clamped between the electrodes. As the upper and lower arms are identical lengthwise as well as status wise, J_U and J_L become identical in magnitude and opposite in sign. In our formulation, positive sign is assigned when current flows in the clockwise direction. The nature of the density profile depends on many factors associated with the junction setup. For a symmetric junction configuration, the peaks are uniform around the discrete energy eigenvalues, and their widths are primarily controlled by the ring-electrode coupling strengths, τ_S and τ_D . For the weak-coupling limit ($\tau_{S(D)} \ll t$), the widths are narrow, while they get broadened in the strong-coupling limit which is specified by the condition $\tau_{S(D)} \sim t$. Since this coupling effect is quite well-known in the context of electron transmission, here it is not explicitly discussed (interested readers can follow the Refs.^{52,53}). Based on the nature of J_U and J_L (Fig. 2(a)), the behavior of J_c (Fig. 2(b)) is easily understood. Across the entire energy window the net circular density becomes zero, and hence, bias driven circular current is not expected for this case i.e., when the upper and lower arms are symmetric to each other.

The circular current can be generated by breaking the symmetry between the two arms, and here it is done by introducing disorder in the backbone sites. As stated earlier, disorder is introduced at all backbone sites while keeping the ring sites free from disorder. In the presence of disorder, the site energies of all backbone sites (N_B)

vary from one another, resulting in different disorder sequences in the two arms. If the sequences are identical in these two arms, applying disorder becomes meaningless, since, in that condition, the arms remain symmetric to each other, resulting in a vanishing net current density, just like in the perfect case stated above. Without

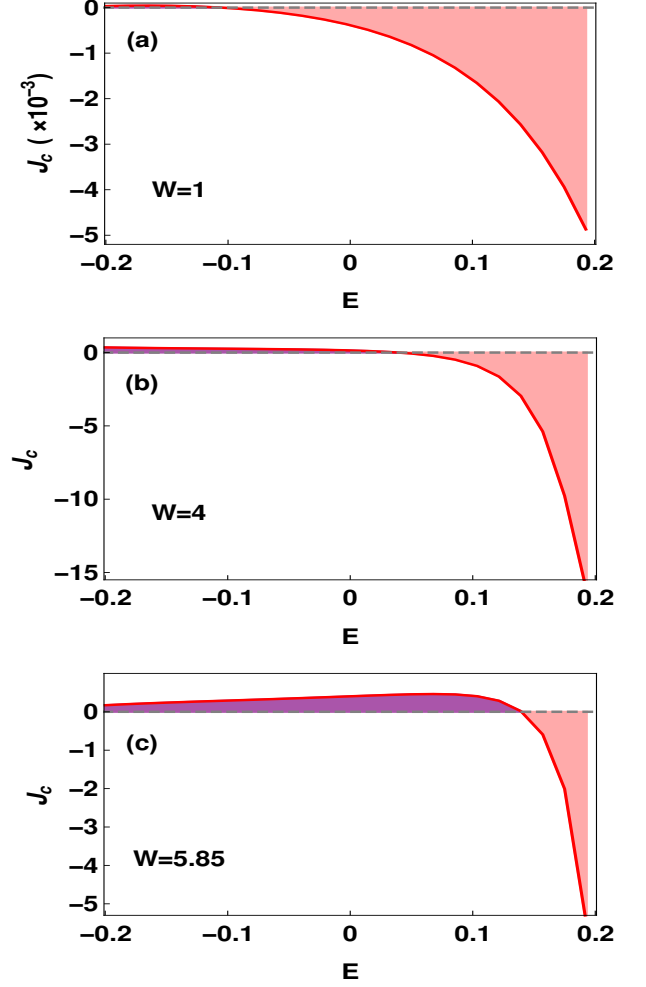


FIG. 4: (Color online). Circular current density J_c as a function of energy for three different values of W corresponding to points A, B, and C on the cyan curve in Fig. 3. Color shading is used to highlight the areas under the curves, with two different colors indicating the areas above and below the $E = 0$ line.

presenting density profiles, like what are shown for the disorder-free case in Fig. 2, in Fig. 3 we directly present the dependence of circular current, computed at a particular bias voltage, as a function of backbone disorder strength W , since our main concern is to explore the effect of backbone disorder. The results are shown for three distinct voltages. Several important features are available. The overall impression is that the circular current becomes vanishingly small for lower values of W , and then it starts increasing with W and after reaching a maximum it decreases and drops close to zero for too large W . This pattern is reflected from all the three curves computed at three distinct biases. This is one of our central results, and here we explain the nature of the

curves for different regimes of W . We choose three points in the cyan curve (other curves can also be taken into account) associated with three different values W , low, moderate and high, that are represented by A, B and C respectively. For these three cases of W , the variations of total circular current density J_c are shown in Fig. 4 (exact values of W are mentioned in the sub-figures). The particular energy window from -0.2 to $+0.2$ is used since $V = 0.4$ V and temperature is fixed at zero. When $W = 1$, corresponding to A point, the current density is extremely small for the entire energy window (Fig. 4(a)), and naturally, I_c becomes vanishingly small. On the other hand, for moderate W ($W = 4$), J_c is appreciable and most importantly it is highly asymmetric around $E = 0$ (or we can say across $J_c = 0$ line) (Fig. 4(b)). The net area of the J_c - E curve is thus reasonably large yielding a higher circular current. Finally when we reach

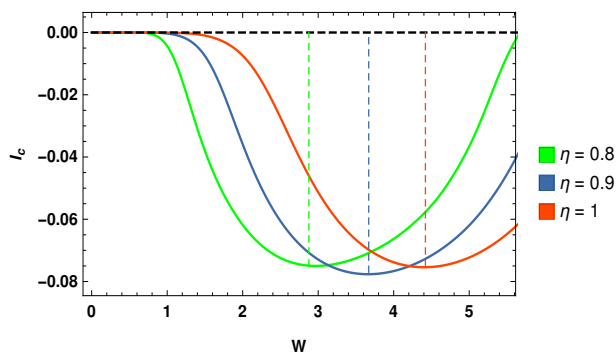


FIG. 5: (Color online). Effect of ring-backbone coupling. I_c - W curves at three typical values of η when the bias voltage is set at 0.5 V. A dashed vertical line is drawn in each curve to clearly locate its extremum point.

to the very large value of W (denoting the C point), it is seen from Fig. 4(c) that the positive and negative areas under J_c - E curves are quite comparable, resulting in a smaller circular current, like the weak W limit. Thus, from the behavior of current density profile, the nature of circular current with W can be clearly understood. Now, it is also important to explain these characteristic features of I_c in different disorder regimes with proper ‘physical arguments’ which are as follows. As already pointed out, the primary requirement to have a finite I_c is to break the symmetry between the upper and lower arms. For $W = 0$, all the backbone sites are uniform and the arms become symmetric. Once the backbone disorder is introduced, the symmetry is lost, but for weak W the symmetry breaking effect is too small. At the same time, within our selected energy window, there are almost no peaks or dips in J_c , resulting in a vanishingly small current. With increasing W , the arms become more asymmetric relative to each other and therefore we get higher circular current with W . The situation becomes counterintuitive beyond a critical disorder where the currents gets reduced with the enhancement of W . This can be interpreted from the concept of an ordered-disordered scenario⁵⁰. The system which is clamped between the electrodes contains two regions. In one region (ring) all the sites are ordered, while for the other region the sites

are disordered, and these two regions are coupled to each other. For weak W , the ordered region is affected by the disordered part, and this effect increases with W which is easy to understand. But the fact is that the coupling between the two regions⁵⁰ gets weakened with increasing W , and for large enough W the ring part is almost decoupled from the backbone sites. In that case, the symmetry between the upper and lower arms of the ring is restored, resulting in a vanishing I_c .

Since the nature of circular current is greatly influenced by the interaction between the ordered region i.e., the ring system and the disordered backbone region, here it is important to check the effect of η on I_c . In Fig. 5 we plot I_c as a function of W at three typical values of η considering the lengthwise symmetric ring nanojunction with $N_R = 10$. All the three curves appear identical

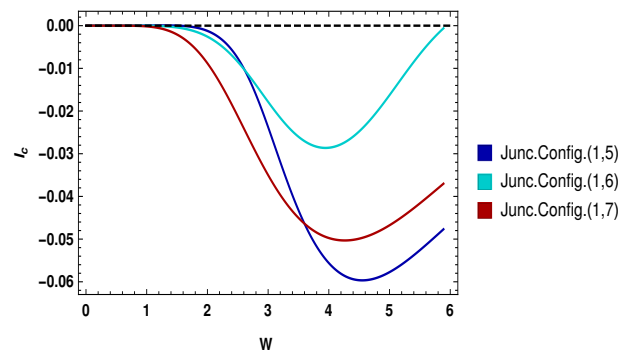


FIG. 6: (Color online). Effect of ring-electrode interface geometry. Variation of I_c as a function of backbone disorder W for three different junction configurations. Along with the length-wise symmetric configuration, two asymmetric configurations are considered where the drain is coupled to sites 5 and 7 respectively of a 10-site ring. Here we set $V = 0.4$ V.

in nature. The key observation is that, the critical W , where I_c reaches its extremum, shifts towards higher W with increasing η . The underlying mechanism depends on the strength of the connection between the ordered and disordered parts. A stronger connection requires a higher W to decouple these two regions, from which point the symmetry between the two arms of the ring begins to reemerge.

The atypical behavior of I_c with W which is discussed above perfectly holds for the other ring-electrode junction configurations as well, which we claim from the curves shown in Fig. 6. In this figure, three junction configurations are taken into account, two are length-wise asymmetric and one for length-wise symmetric, and the results are worked out for a typical bias voltage $V = 0.4$ V. Along with these, some other configurations are also checked and in each case the dependence of W on I_c remains exactly same. It is well-known that ring-electrode configuration plays a significant role on transport behavior, due to the modification of quantum interference of the wave functions associated with different branches of the ring, and therefore, the maxima points (in the -ve side of each curve) get shifted, but the overall response of I_c with W is unchanged.

To inspect the robustness i.e., whether the above dis-

cussed nature is specific to AAH type disorder or it is general with respect to the other type of backbone disorder, here we check the behavior of I_c - W curve in presence of other types of backbone disorder. We choose two different types of disorder in backbone sites: one is the Fibonacci type, and the other is the Bronze Mean (BM) one^{36–38}. These are quite common examples of correlated disorders and they can be constructed using two different kinds of atomic sites, say A and B , by arranging them according to specific rules^{36–38}, unlike AAH type where all the sites are different. The inflation rule for the Fibonacci

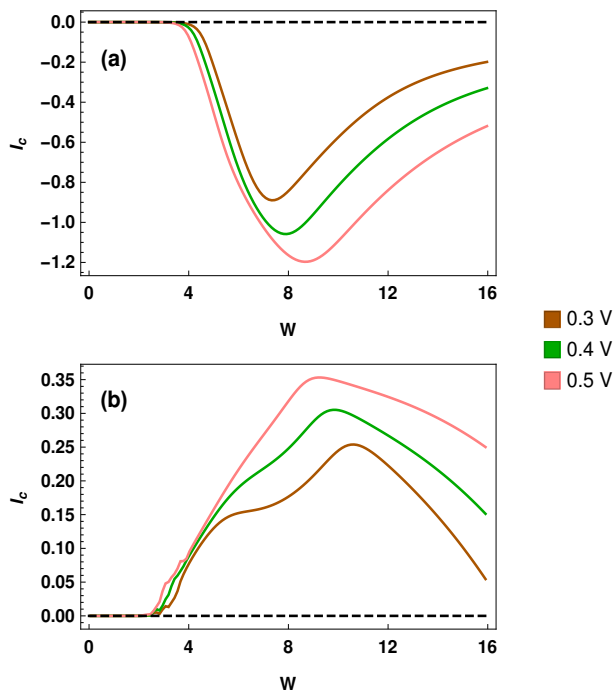


FIG. 7: (Color online). I_c - W characteristics at three typical bias voltages for the ring system with (a) Fibonacci type backbone disorder and (b) BM type backbone disorder. Here we choose $N_R = 13$, and connect the source and drain electrodes so that the length difference between the upper and lower arms equals the length of a single bond. The other physical parameters are: $t_0 = 5$, $\tau_S = \tau_D = 2$, $t = 2$, $\eta = 2$, and $\epsilon_A = -\epsilon_B = 0.5$.

sequence is: $A \rightarrow AB$ and $B \rightarrow A$. So the first few Fibonacci generations are A , AB , ABA , $ABAAB$, etc. On the other hand, the inflation rule for the BM sequence is: $A \rightarrow AAAB$ and $B \rightarrow A$, and here the first few generations are: A , $AAAB$, $AAABAAABAAABA$, etc. For these two different atomic sites (A and B) we refer the site energies ϵ_A and ϵ_B respectively, and their strengths are specified by the parameter W (like the AAH case). Inserting the Fibonacci and BM disorders in the backbone sites, the variations of circular current with respect to W are shown in Fig. 7. Here we consider a 13-site ring, to have a comparative ring size with our previously studied AAH case (10-site rings cannot be obtained with these sequences). As the ring size is odd, identical arm lengths are not possible, and we couple the electrodes in such a way that the length difference between the two arms is just a single bond. For this particular figure

(Fig. 7), the chosen TB parameters are also quite different compared to the other figures. It is just because to capture all the information within the varied W window. We make t_0 quite large, and thus, we proportionately change other parameters such that energy band widths of the electrodes are larger than the system placed between them. In each type of backbone disorder, the variation of I_c with W is shown for three distinct bias voltages, and both for the two types of disorders the nature of I_c with W remains exactly similar with what is already obtained for the AAH case. The only difference is the

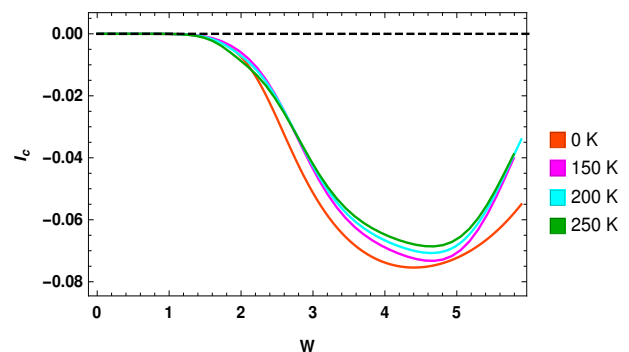


FIG. 8: (Color online). Effect of temperature. Variation of I_c for the ring system possessing AAH type backbone disorder as a function of W at three different temperatures. The result of zero temperature is superimposed for a clear comparison. Here we take $N_R = 10$, $\eta = 1$ and $V = 0.5$ V. The electrodes are coupled in a lengthwise symmetric configuration.

sign reversal. The circular current can have both positive and negative signs (unlike transport current which always exhibits one sign for a particular polarity) as it depends on the contributing peaks and dips in the current density profile. The sign of I_c depends on which dominates among the peaks and dips of J_c . Figure 7 clearly suggests that the overall signature of I_c with W remains unchanged with the type of disorder. Here we would like to note that, in addition to these three distinct types of disorder, the behavior of I_c remains the same with other different backbone configurations which we firmly confirm through our detailed numerical calculations, and to avoid any repetition, we do not add those results.

For our chosen quantum system, it is established that electrical conduction can be monitored in different ways. In particular, backbone disorder plays a crucial role, as it causes the system to map onto an ordered-disordered separated structure, where the coupling between the ordered and disordered regions is significant. Other influential factors include the ring-electrode junction configuration, which directly affects quantum interference, and the ring-electrode coupling. The latter can be selectively tuned in a suitable laboratory setting and has already been examined in various junction setups.

The results analyzed so far are computed for zero temperature. For a more realistic scenario it is also crucial to examine the role of temperature. The temperature dependence enters into the current expression through the Fermi-Dirac distribution functions, f_S and f_D , associated with the source and drain electrodes, respectively.

The effect of temperature is presented in Fig. 8, where I_c - W curves are shown for three distinct temperatures. The result of zero temperature is also superimposed for comparison. Apart from a slight reduction of current with temperature, we find that the overall nature of I_c - W curve remains unaltered. The reduction of current due to temperature can be understood from the following arguments. At absolute zero temperature, the current is obtained by integrating the current density profile within

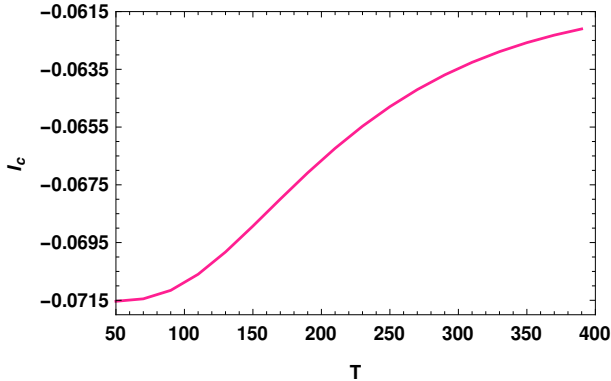


FIG. 9: (Color online). Dependence of I_c with temperature (measured in Kelvin) for the identical setup as mentioned in Fig. 8. Here W is fixed at 4 eV.

the energy window from $E_F - eV/2$ to $E_F + eV/2$. Within this energy zone, depending on the dominating peaks and dips we get the net current. Here the chance of mutual cancellations is relatively less. On the other hand, when the temperature is finite, we need to consider the full available energy window where the chance of mutual cancellations may slightly increase though it depends on many other factors, especially W , and depending on the weight factor ($f_S - f_D$) we get the resultant current.

A more comprehensive dependence of I_c on temperature is given in Fig. 9, where the variation of I_c at a particular voltage is shown by continuously changing the temperature in a broad range. A smooth reduction of I_c with temperature is obtained, following the above arguments. The key aspect is that, I_c remains finite even at very high temperatures.

■ Possible ways to detect bias driven circular current: It is quite significant to explore how bias driven circular current can be verified through experimental observations. Detecting such effects in a practical setting presents both challenges and opportunities. Two possible approaches can be considered¹⁰ for their experimental observation. The first approach involves examining the spectral response of magnetic ions that are positioned either on or near the quantum ring. These ions interact with the local magnetic field induced in their vicinity due to the circular current, and their spectral characteristics can reveal valuable information about the underlying magnetic effects. The second approach focuses on the response of local magnetic moment that develops within the ring itself to an external magnetic field. By studying the behavior of magnetic moment, it is possible to infer details of the induced magnetic field generated by the

bias driven circular current. Both methods offer promising avenues for experimentally probing this theoretically studied phenomenon, bridging the gap between theoretical predictions and real experimental observations.

■ Possible design prescriptions for the junction: Here, it is pertinent to briefly describe how our proposed quantum system can be designed in the laboratory. The system consists of two main components: a nano ring and backbone sites. Several novel strategies are available for fabricating a nano ring, including electron-beam lithography^{54,55}, ion beam milling^{56,57}, UV lithography^{58,59}, annealing techniques^{60,61}, and more. The backbone sites, which can be considered discrete quantum dots (QDs), are positioned such that each ring site is connected to one backbone site via a tunnel junction. Using suitable gate electrodes, the coupling strength between the ring and the backbone sites can be controlled. Additionally, the backbone site energies can be modulated, either randomly or deterministically, through local gate voltage variations or laser-induced potential fluctuations.

IV. CLOSING REMARKS

In this work, we examine the critical role of environmental interactions on bias-driven circular currents in a nano ring. The environmental effects are phenomenologically incorporated by connecting the ring sites to disordered backbone sites, each directly coupled to a parent lattice site of the ring via a single bond. The ring is sandwiched between two contact electrodes, source and drain. When a finite bias is applied between these electrodes, a net circular current is induced in the ring. The characteristics of this current are studied in detail under various input conditions.

Using a tight-binding framework to describe the quantum system, all results are derived based on wave-guide theory. The effect of backbone disorder is particularly noteworthy. As the disorder strength increases, the current magnitude initially rises, reaches a maximum, and then decreases, eventually vanishes at very high disorder strengths. These behaviors are thoroughly analyzed with appropriate mathematical results and physical explanations. Additionally, it is established that the effect of disorder remains largely unchanged regardless of the type of disorder. Temperature dependence is also discussed considering a more realistic scenario, showing that significant current can still be obtained over a wide temperature range. At the end, we briefly discuss the detection mechanisms of bias driven circular current and highlight possible strategies for realizing our proposed model in a suitable laboratory.

Finally, we emphasize that if environmental interactions is controlled through suitable laboratory methods, transport behavior can be selectively regulated. This potential for control is highly interesting and important. Moreover, controlling the spin-dependent bias-driven circular current through environmental interaction presents another intriguing phenomenon. Various spin-dependent scattering factors can be considered⁶²⁻⁶⁶, such as spin-

moment interactions in magnetic systems, spin-orbit interactions, Zeeman splitting, etc. In each case, distinct non-trivial signatures can be expected. These aspects will be explored in our forthcoming work.

Appendix A: Coupled equations involving wave amplitudes at different lattice sites

Referring to Fig. 10, which illustrates a 6-site ring coupled to source and drain electrodes, here we express all

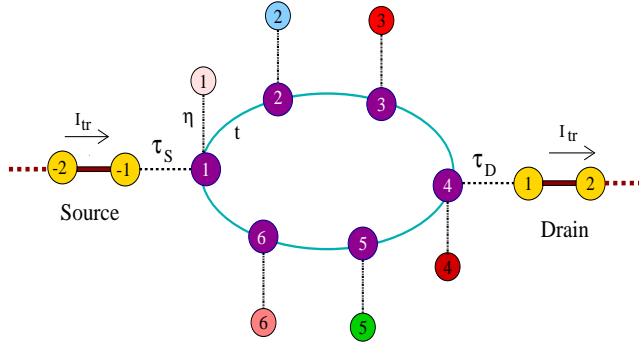


FIG. 10: (Color online). Schematic diagram of a ring nano-junction, where a six-site ring is coupled to one-dimensional source and drain electrodes. These electrodes are attached to sites 1 and 4 of the ring. Each site of the ring is further connected to a backbone site through a single bond.

14 equations corresponding to the 14 lattice sites – 6 associated with the ring sites, 6 with the backbone sites, and the remaining 2 with the side-attached electrodes. For the electrodes, these two sites are site number –1 of

S and site number 1 of D, as these two sites are directly coupled to the ring sites. The equations are as follows:

$$\begin{aligned}
 (E - \epsilon_{R,1}) C_{R,1} &= tC_{R,2} + tC_{R,6} + \eta C_{B,1} + \tau_S C_{S,-1}, \\
 (E - \epsilon_{R,2}) C_{R,2} &= tC_{R,1} + tC_{R,3} + \eta C_{B,2}, \\
 (E - \epsilon_{R,3}) C_{R,3} &= tC_{R,2} + tC_{R,4} + \eta C_{B,3}, \\
 (E - \epsilon_{R,4}) C_{R,4} &= tC_{R,3} + tC_{R,5} + \eta C_{B,4} + \tau_D C_{D,1}, \\
 (E - \epsilon_{R,5}) C_{R,5} &= tC_{R,4} + tC_{R,6} + \eta C_{B,5}, \\
 (E - \epsilon_{R,6}) C_{R,6} &= tC_{R,5} + tC_{R,1} + \eta C_{B,6}, \\
 (E - \epsilon_{B,1}) C_{B,1} &= \eta C_{R,1}, \\
 (E - \epsilon_{B,2}) C_{B,2} &= \eta C_{R,2}, \\
 (E - \epsilon_{B,3}) C_{B,3} &= \eta C_{R,3}, \\
 (E - \epsilon_{B,4}) C_{B,4} &= \eta C_{R,4}, \\
 (E - \epsilon_{B,5}) C_{B,5} &= \eta C_{R,5}, \\
 (E - \epsilon_{B,6}) C_{B,6} &= \eta C_{R,6}, \\
 (E - \epsilon_{S,-1}) C_{S,-1} &= \tau_S C_{R,1} + t_0 C_{S,-2}, \\
 (E - \epsilon_{D,1}) C_{D,1} &= \tau_D C_{R,4} + t_0 C_{D,2}.
 \end{aligned} \tag{A1}$$

Assuming a plane wave incidence of unit amplitude from the source end, the wave amplitude at m th site of the source electrode can be expressed as $C_{S,m} = e^{ik(m+1)} + re^{-ik(m+1)}$, while for the outgoing wave in the drain electrode, the wave amplitude is given by $C_{D,m} = \tau e^{ikm}$. Here r and τ denote the reflection and transmission amplitudes, respectively, and k is the wave vector related to the TB parameters through the energy dispersion relation $E = \epsilon_0 + 2t_0 \cos(k)$. By solving the above equations, we find all the required coefficients as a function of energy E .

-
- * Electronic address: santanu.maiti@isical.ac.in
- ¹ S. Nakanishi and M. Tsukada, Jpn. J. Appl. Phys. **37**, L1400 (1998).
 - ² S. Nakanishi and M. Tsukada, Phys. Rev. Lett. **87**, 126801 (2001).
 - ³ M. Ernzerhof, H. Bahmann, F. Goyer, M. Zhuang, and P. Rocheleau, J. Chem. Theory Comput. **2**, 1291 (2006).
 - ⁴ N. Tsuji, S. Takajo, and H. Aoki, Phys. Rev. B **75**, 153406 (2007).
 - ⁵ K. Tagami, M. Tsukada, W. Yasuo, T. Iwasaki, and H. Nishide, J. Chem. Phys. **119**, 7491 (2003).
 - ⁶ E. Y. Soto-Gómez, J. H. O. Silva, J. A. Gil-Corrales, D. Gallego, M. F. H. Morales, A. L. Morales, and C. A. Duque, Condens. Matter **8**, 60 (2023).
 - ⁷ J. H. O. Silva, J. C. C. Penaranda, J. A. G. Castano, and C. A. Duque, Molecules **23**, 881 (2018).
 - ⁸ J. H. Ojeda, C. A. Duque, and D. Laroze, Org. Electron. **41**, 369 (2017).
 - ⁹ M. Dey, S. K. Maiti, and S. N. Karmakar, Org. Electron. **12**, 1017 (2011).
 - ¹⁰ D. Rai, O. Hod, and A. Nitzan, J. Phys. Chem. C **114**, 20583 (2010), and the references therein.
 - ¹¹ D. Rai, O. Hod, and A. Nitzan, Phys. Rev. B **85**, 155440 (2012).
 - ¹² M. Patra and S. K. Maiti, Sci. Rep. **7**, 43343 (2017).
 - ¹³ S. Ganguly and S. K. Maiti, J. Phys.: Condens. Matter **33**, 045301 (2020).
 - ¹⁴ U. Dhakal and D. Rai, J. Phys.: Condens. Matter **31**, 125302 (2019).
 - ¹⁵ Y. J. Xiong and X. T. Liang, Phys. Lett. A **330**, 307 (2004).
 - ¹⁶ M. Mondal and S. K. Maiti, Europhys. Lett. **146**, 56003 (2024).
 - ¹⁷ D. K. Suhendro, E. Yudiarsah, and R. Saleh, Physica B **405**, 4806 (2010).
 - ¹⁸ D. Klotsa, R. A. Römer, M. S. Turner, Biophys. J. **89**, 2187 (2005).
 - ¹⁹ J. X. Zhong, in: B. Romamowicz, M. Laudon (Eds.), Proceedings of the 2003 Nanotechnology Conference, Computational Publications, vol. 2, p. 105 (2003).
 - ²⁰ A. -M. Guo, Z. Yang, H. -J. Zhu, and S. -J. Xiong, J. Phys.: Condens. Matter **22**, 065102 (2010).
 - ²¹ A. -M. Guo, S. -J. Xiong, Z. Yang, and H. -J. Zhu, Phys. Rev. E **78**, 061922 (2008).
 - ²² E. Maciá, S. Roche, Nanotechnology **17**, 3002 (2006).
 - ²³ S. Kundu and S. N. Karmakar, Phys. Lett. A **379**, 1377 (2015).
 - ²⁴ P. W. Anderson, Phys. Rev. **109**, 1492 (1958).
 - ²⁵ P. A. Lee and T. V. Ramakrishnan, Rev. Mod. Phys. **57**, 287 (1985) and the references therein.

- ²⁶ N. Mott, J. Phys. C **20**, 3075 (1987).
- ²⁷ E. Abrahams, P. W. Anderson, D. C. Licciardello, and T. V. Ramakrishnan, Phys. Rev. Lett. **42**, 673 (1979).
- ²⁸ B. Hetényi, S. Parlak, and M. Yahyavi, Phys. Rev. B **104**, 214207 (2021).
- ²⁹ J. C. Flores, J. Phys.: Condens. Matter **1**, 8471 (1989).
- ³⁰ S. Aubry and G. Andre, Ann. Israel Phys. Soc. **3**, 133 (1980).
- ³¹ P. G. Harper, Proc. Phys. Soc. A **68**, 874 (1955).
- ³² M. Verbin, O. Zilberberg, Y.E. Kraus, Y. Lahini, Y. Silberberg, Phys. Rev. Lett. **110**, 076403 (2013).
- ³³ Y. E. Kraus, Y. Lahini, Z. Ringel, M. Verbin, and O. Zilberberg, Phys. Rev. Lett. **109**, 106402 (2012).
- ³⁴ J. Biddle and S. Das Sarma, Phys. Rev. Lett. **104**, 070601 (2010).
- ³⁵ S. Sil, S. K. Maiti, and A. Chakrabarti, Phys. Rev. Lett. **101**, 076803 (2008).
- ³⁶ M. Saha and S. K. Maiti, Physica E **93**, 275 (2017).
- ³⁷ A. M. Guo, Phys. Rev. E **75**, 061915 (2007).
- ³⁸ H. Lei, J. Chen, G. Nouet, S. Feng, Q. Gong, and X. Jiang, Phys. Rev. B **75**, 205109 (2007).
- ³⁹ M. S. S. Junior, W. V. P. de Lima, V. A. Teixeira, D. B. da Fonseca, F. Moraes, A. L. R. Barbosa, G. M. A. Almeida, F. A. B. F. de Moura, J. Magn. Magn. Mater. **579**, 170880 (2023).
- ⁴⁰ F. M. Izrailev, A. A. Krokhin, and N. M. Makarov, Phys. Rep. **512**, 125 (2012).
- ⁴¹ S. Thébaud, L. Lindsay, and T. Berlijn, Phys. Rev. Lett. **131**, 026301 (2023).
- ⁴² A. R. C. Buarque, W. S. Dias, G. M. A. Almeida, M. L. Lyra, and F. A. B. F. de Moura, Phys. Rev. A **107**, 012425 (2023).
- ⁴³ S. Ganguly and S. K. Maiti, Sci. Rep. **13**, 13633 (2023).
- ⁴⁴ R. Bhattacharya and S. K. Maiti, Annalen der Physik **534**, 2200190 (2022).
- ⁴⁵ M. Sarkar, S. K. Maiti, and M. Dey, J. Phys.: Condens. Matter **34**, 195303 (2022).
- ⁴⁶ M. Dey, S. Chakraborty, and S. K. Maiti, J. Phys. D: Appl. Phys. **55**, 085302 (2022).
- ⁴⁷ L. -Y. Gong, Y. -G. Ding, and Y. -Q. Deng, Chinese Phys. B **26**, 117201 (2017).
- ⁴⁸ G. M. A. Almeida, R. F. Dutra, A. M. C. Souza, M. L. Lyra, and F. A. B. F. de Moura, Phys. Rev. B **108**, 022407 (2023).
- ⁴⁹ G. Xiong, Phys. Rev. B **76**, 153303 (2007).
- ⁵⁰ J. Zhong and G. M. Stocks, Nano Lett. **6**, 128 (2006).
- ⁵¹ M. Rossignolo and L. Dell’Anna, Phys. Rev. B **99**, 054211 (2019).
- ⁵² K. Walczak, Phys. Status Solidi (b) **241**, 2555 (2004).
- ⁵³ S. K. Maiti, Physica E **36**, 199 (2007).
- ⁵⁴ L. Berger, J. Jurczyk, K. Madajska, I. B. Szymanska, P. Hoffmann, and I. Utke, Micromachines **12**, 580 (2021).
- ⁵⁵ M. Y. Fominsky, L. V. Filippenko, A. M. Chekushkin, P. N. Dmitriev, V. P. Koshelets, Electronics **10**, 2944 (2021).
- ⁵⁶ F. I. Allen, Micromechanics **12**, 232 (2021).
- ⁵⁷ M. Manoccio, M. Esposito, A. Passaseo, M. Cuscuna, and V. Tasco, Micromachines **12**, 6 (2021).
- ⁵⁸ T. Manouras and P. Argites, Nanomaterials **10**, 1593 (2020).
- ⁵⁹ A. L. Grab, A. Bacher, A. Nesterov-Mueller, and R. Dahnit, Bioengineering **9**, 63 (2022).
- ⁶⁰ P. Potejanasak and S. Duangchan, Crystals **10**, 533 (2020).
- ⁶¹ G. Barrera, F. Celegato, M. Cialone, M. Coisson, P. Rizzi, and P. Tiberto, Sensors **21**, 7420 (2021).
- ⁶² B. S. Kandemir and D. Akay, Philosophical Magazine **97**, 2225 (2017).
- ⁶³ B. S. Kandemir and D. Akay, Phys. Status Solidi B **255**, 1800163 (2018).
- ⁶⁴ B. S. Kandemir and D. Akay, J. Magn. Magn. Mater. **384**, 101 (2015).
- ⁶⁵ S. Sarkar and S. K. Maiti, Phys. Rev. B **100**, 205402 (2019).
- ⁶⁶ D. Das Gupta and S. K. Maiti, Phys. Rev. B **106**, 125420 (2022).